

See discussions, stats, and author profiles for this publication at: <https://www.researchgate.net/publication/253526163>

Characterization of heterogeneities from core X-ray scans and borehole wall images in a reefal carbonate reservoir: influence on the porosity structure

Article · April 2009

CITATIONS

0

READS

165

7 authors, including:



Vaness Hebert

Université de Montpellier

8 PUBLICATIONS 29 CITATIONS

[SEE PROFILE](#)



Charlotte Garing

University of Georgia

17 PUBLICATIONS 121 CITATIONS

[SEE PROFILE](#)



Philippe Adrien Pezard

French National Centre for Scientific Research

190 PUBLICATIONS 2,384 CITATIONS

[SEE PROFILE](#)



Yves G. Maria-Sube

Yves Maria-Sube

5 PUBLICATIONS 7 CITATIONS

[SEE PROFILE](#)

Some of the authors of this publication are also working on these related projects:



Deep drilling of ocean basement 1: DSDP/ODP Hole 504B (equatorial Pacific Ocean) [View project](#)



Microbial Communities General [View project](#)

Multi-scale X-ray tomography analysis of carbonate porosity

V. HEBERT, C. GARING*, L. LUQUOT, P. A. PEZARD & P. GOUZE

Géosciences Montpellier, UMR 5243 CNRS/INSU, Université de Montpellier 2, 34095 Montpellier, France

**Corresponding author (e-mail: Charlotte.Garing@gm.univ-montp2.fr)*

Abstract: The porosity (from values of <1% up to more than 50%, with a mean value of 36.5%) and permeability (from very low values to 20.4 D, with a mean value around 800 mD) of 38 plugs, with a diameter 40 mm, have been measured. These plugs were taken approximately every 1.5 m along a 100 m-long core, sampling a series of reefal carbonate platform lithofacies. A non-unique relationship between porosity and permeability is obtained. In addition, the porosity was measured from processing X-ray micro-tomography images with resolutions ranging from 0.42 to 190.0 μm and sampling volumes ranging from less than 1 μm^3 to few cm^3 . Depending on the structure of the pore network, the computed porosity is, in some cases, controlled by the X-ray image resolution and the sampled volume. While high resolution is required to image micro-porous material, large samples with lower resolution images are necessary for identifying distributed vugs and millimetre-scale structures. This study shows that multi-resolution X-ray micro-tomography is an effective tool for characterizing the multi-scale pore structure of carbonate rocks and understanding how it may control key petrophysical parameters such as porosity and permeability.

Carbonate reservoirs are known to be heterogeneous over a wide range of scales. The heterogeneity arises from complex sedimentary and diagenetic processes (e.g. Mazzullo & Chilingarian 1992; Moore 2001; Mylroie & Carew 2003). As a result, carbonates exhibit widely varying petrophysical properties (porosity, permeability, diffusivity) that can vary over very short distances within the reservoir. This heterogeneity renders carbonate rocks and carbonate reservoirs difficult to characterize from a petrophysical point of view, and affects our ability to distribute and upscale these petrophysical properties in static geological models of carbonate reservoirs. Novel approaches are hence required to better understand the relationship between the heterogeneous nature of the rock and flow properties. Such novel approaches include the use of X-ray computed tomography (CT) imaging. X-ray CT imaging provides a means to characterize the pertinent pore-scale properties (e.g. pore-size distribution, tortuosity, connectivity) and to quantify how these microscopic properties influence the macroscopic properties (e.g. permeability, porosity, relative permeability).

Several pore classifications and rock-typing schemes have been proposed to relate rock texture and pore type to petrophysical properties (e.g. Archie 1952; Choquette & Pray 1970; Lucia 1983, 1995; Lonoy 2006; Clerke *et al.* 2008; Hollis *et al.* 2010; Van der Land *et al.* 2013). Although progress has been made in reservoir rock typing, carbonate rocks still present significant challenges. Carbonate rocks often display widely varying electric, acoustic or hydrodynamic properties, even for similar

porosity ranges and pore-type classification; conversely, carbonates with distinctly different pore geometry can also have different petrophysical properties (Weger *et al.* 2009; Hollis *et al.* 2010; Verwer *et al.* 2011; Vialle & Vanorio 2011; Garing *et al.* 2013b; Van der Land *et al.* 2013).

Reservoir-scale structures and layers are traditionally imaged using geophysical techniques calibrated from downhole measurements. These are mainly indirect measurements, for example either borehole wall images, or electrical, acoustic and nuclear methods. Conversely, these geophysical measurements can be related to the petrophysical properties using direct core measurements (porosity, electrical resistivity, acoustic velocities, permeability, capillary pressure, dispersivity). Complementary parameters such as the void–solid interface area can be assessed by the Brunauer, Emmett and Teller (BET) method (Brunauer *et al.* 1938). The empirical models developed for relating the geophysical, petrophysical and hydrodynamical properties (e.g. the Archie, Wyllie and Kozeny–Carman equations for resistivity–porosity, acoustic velocity–porosity and porosity–permeability relationships, respectively) have been successfully used for sandstone reservoirs. However, whether these traditional relationships are applicable to carbonates (if at all) remains unclear owing to the intrinsic heterogeneity of carbonates and the associated complexity of pore structures. How to best characterize the hydrodynamic (and other) properties of carbonate rocks and how to upscale them to the reservoir scale remains, therefore, an open question.

Attempts have been made to relate petrophysical and flow properties to two-dimensional (2D) structure characteristics using thin-section analysis (Weger *et al.* 2009; Casteleyn *et al.* 2010; Verwer *et al.* 2011). However, 2D models are inappropriate to quantify the 3D complexity of the pore connectivity that controls permeability because pores are commonly disconnected in two dimensions, especially in carbonates (Nimmo 2004). Hence, new approaches are needed to overcome this challenge (Jiang *et al.* 2013*a, b*; Prodanović *et al.* 2014).

Recent developments in non-destructive imaging techniques, specifically X-ray micro-tomography (XRMT), enable the 3D characterization of the pore structure. This in turn allows us to relate the petrophysical properties measured in the laboratory at macroscale to properties imaged and quantified at pore scale (Lindquist *et al.* 2000; Arns *et al.* 2005; Knackstedt *et al.* 2008; Remeysen & Swennen 2008; Blunt *et al.* 2013; Garing *et al.* 2013*b*). The relationship between porosity and permeability, for example, can be investigated not only from a static point of view (by measuring these two properties from a set of cores) but also from a dynamic point of view by investigating how the pore structure evolves during controlled dissolution experiments (Luquot & Gouze 2009; Noiriél *et al.* 2009; Gouze & Luquot 2011; Varloteaux *et al.* 2013; Luquot *et al.* 2013; Nagues *et al.* 2013; Vialle *et al.* 2013). Petrophysical and transport properties can also be directly computed from XRMT images, which may lead to more robust upscaling methods (Arns *et al.* 2001, 2004, 2005; Knackstedt *et al.* 2008; Dehghan Khalili *et al.* 2013*a, b*). These studies established in principle that X-ray CT imaging is appropriate to analyse how the pore-scale topology controls the macroscopic properties of complex carbonate rocks. However, XMRT imaging techniques suffer from limitations, both in terms of field of view and resolution. These aspects need to be considered when studying rocks displaying scale-dependent heterogeneities such as carbonates. The issue is twofold: first, carbonates often contain noticeable fractions of micro-porosity that cannot be resolved at micron-scale resolution. However, using a sub-micron resolution implies that the resulting sample volume is too small to capture the heterogeneity of the macro-porosity. Furthermore, the connectivity of the pore network at the scale of the sample is often controlled by the distribution of the micro-porosity clusters (Garing *et al.* 2013*b*; Mehmani & Prodanovic 2014). In this case, the intrinsic permeability of the micro-porosity clusters will govern the permeability of the entire sample as macro-pores are interconnected by micro-porous material. Consequently, the macro-scale permeability tends to reach the harmonic mean of the macro-pores

and micro-porous material permeability. Accordingly the distribution of the micro-porosity must be measured in parallel to the evaluation of the intrinsic permeability of the micro-porous material. This can be done using imaging techniques with nanometer-scale resolution such as focused ion beam scanning electron microscopes (FIB-SEM) or optimization methods conditioned to a laboratory measurement of porosity (Mangane *et al.* 2013). Similar difficulties are encountered when determining other properties such as those related to acoustic wave propagation or electrical conductivity.

Using pore-scale numerical computations to estimate permeability and other petrophysical properties for multi-scale pore structures is challenging and computationally intensive. At present, solving the Stokes equation directly using grid-based computational fluid dynamics or lattice methods (e.g. gas or Boltzmann methods) remains restricted to samples of relatively small size, even with high-end computing facilities (Zaretskiy *et al.* 2010; Mostaghimi *et al.* 2013). Such samples may contain a few thousand pores, while the complete multi-scale pore volume imaged by standard XRMT techniques typically contains tens to hundreds of thousands of pores. A possible alternative is to use Monte Carlo approaches to account for sample-scale heterogeneities while performing the actual computations on much smaller subvolumes (Sadhukhan *et al.* 2012). Alternatively, pore-network modelling techniques based on simplifications of the actual pore structure to a network of connected pores and throats have been developed during the last decades (Blunt *et al.* 2013). Such approaches are attractive for modelling carbonate rocks because multi-scalar characteristics of the carbonates can be included (Jiang *et al.* 2013*a, b*). Although acceptable for some simple porous media, the representation of the complex geometry of many carbonate rocks (where the distinction between pores and throats is often impossible) makes pore-network models challenging. An alternative approach, the so-called 'hybrid model', is being developed and consists of jointly solving Darcy's equation in regions with micro-porosity and the Stokes equation in the remaining regions.

In summary, there is a series of issues that should be resolved to use XMRT on a regular basis for analysing carbonate pore structures and related petrophysical properties. The key challenge is the characterization and numerical computation of petrophysical properties across all pertinent scales. In this context, the aim of this paper is to evaluate how multi-scale X-ray CT imaging techniques can improve the characterization of heterogeneous carbonate rocks. In particular, our study focuses on the quantification of porosity using

MULTI-SCALE X-RAY TOMOGRAPHY ANALYSIS

multi-resolution XRMT techniques. We also investigate whether this approach is efficient for all pore networks or has limitations for specific types of carbonate pore structures.

Material and methods

The Mallorca experimental site

The field site of this study is located at Ses Sitjoles, in the SE part of Mallorca Island, 6 km away from the coast (Fig. 1). The site, where a dozen 100 m-deep boreholes have been drilled and seven of them fully cored, has been used for several geological, petrophysical, geophysical, geochemical or hydrodynamical studies (Jaeggi 2006; Maria-Sube 2008; Gouze *et al.* 2008, 2009; Pezard *et al.* 2009; Garing 2011; Hebert 2011; Garing *et al.* 2013a, b). The reservoir encountered at Ses Sitjoles belongs to the inland part of the Lluçmajor reef-rimmed platform that formed during the Miocene. Several tectonic and diagenetic events affected the reservoir during the Miocene and Pleistocene. The changes of carbonate production and accommodation related to high-frequency sea-level fluctuations resulted in a complex facies architecture of the platform (Pomar 2001). The large-scale structure of the prograding Miocene reef body,

which exhibits spectacular outcrops at the coast, has been extensively described (Esteban 1979, Pomar *et al.* 1996, Pomar & Ward 1999).

The lithology of the Ses Sitjoles site is characterized by upwards foreereef to lagoonal depositional environments. The foreereef sediments, located from 61.7 to 100.0 m below surface (mbs) in hole MC2, consist of fine-grained packstones–rudstones. This foreereef unit is overlain, from 25 to 61.7 mbs, by reef barrier formations with a dominant framework of coral build-ups with bioclastic infills and massive coral-algal build-ups. The shallowest units, from 0 to 25 mbs, are sediments that accumulated in an inner platform environment. They comprise skeletal grainstones and packstones, muddy limestones, clays, and oolitic grainstones (Hebert 2011).

The current water table at Ses Sitjoles is located near 38 mbs. Owing to the presence of a massive seawater intrusion that is presently invading the aquifer up to 10 km from the coast, the freshwater saturating the barrier reef unit becomes brackish in the foreereef unit at about 62 mbs, and reaches salinity values similar to that of seawater at 80 mbs. Garing *et al.* (2013a) investigated the geochemical characteristics of the mixing zone and reported on-going calcite dissolution enhanced by microbiological activity.

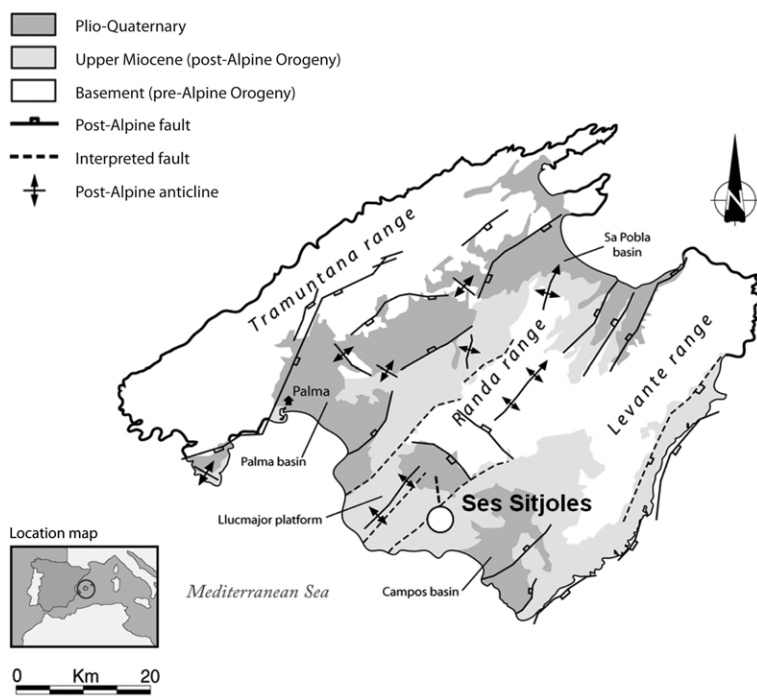


Fig. 1. Geological map of Mallorca Island, Spain, and the location of the Ses Sitjoles site.

The variability of the facies and the diagenetic events have significantly modified the depositional rock fabric, which resulted in highly heterogeneous and complex porosity distributions across many scales, with alternating indurated low porous cemented layers and dissolution cavities of variable size, especially in the inner platform and reef barrier units (Fig. 2).

Samples

Fifty-five carbonate samples from the core taken at Ses Sitjoles in the MC10 hole are used in this study. Thirty-eight 40 mm-diameter plugs, 60 mm in length, named ‘macroplugs’, were regularly sampled from the MC10 core. The porosity and permeability of each macroplug was measured by performing gas injection tests. The pore volume of the core sample is computed by measuring the change in helium pressure and applying Boyle’s law (Nimmo 2004). The permeability is computed by measuring the pressure drop induced by the injection of nitrogen through the plug at different gas pressures (i.e. different flow rates) and using

Darcy’s law. The permeability values are then corrected from the Klinkenberg gas slippage effect (Klinkenberg 1941). The values are given in milli-Darcys ($1 \text{ mD} = 0.97 \times 10^{-15} \text{ m}^2$).

A set of 17 smaller plugs (eight 9 mm-diameter plugs, 18 mm in length and named ‘mini-plugs’, and nine 2 mm-diameter plugs, 8 mm in length and named ‘microplugs’) was also sampled from the MC10 core in the vicinity of each macroplug. The miniplugs and microplugs, listed in Table 1 and illustrated in Figure 3, are classified into three groups depending on their pore types. Samples M1–M7 display a high moldic porosity, and a noticeable interparticle and intraparticle microporosity in the matrix and cements. Samples V1–V4 are characterized by a large number of macroscopic vugs in a cemented matrix. Samples I1–I6 are formed by a micro-porous matrix. Samples I1 and I2 contain few macro-pores (vugs, molds) and fissures.

All of the samples (macroplugs, miniplugs and microplugs) were imaged using X-ray computed tomography (XRCT) or XRMT, as detailed below.

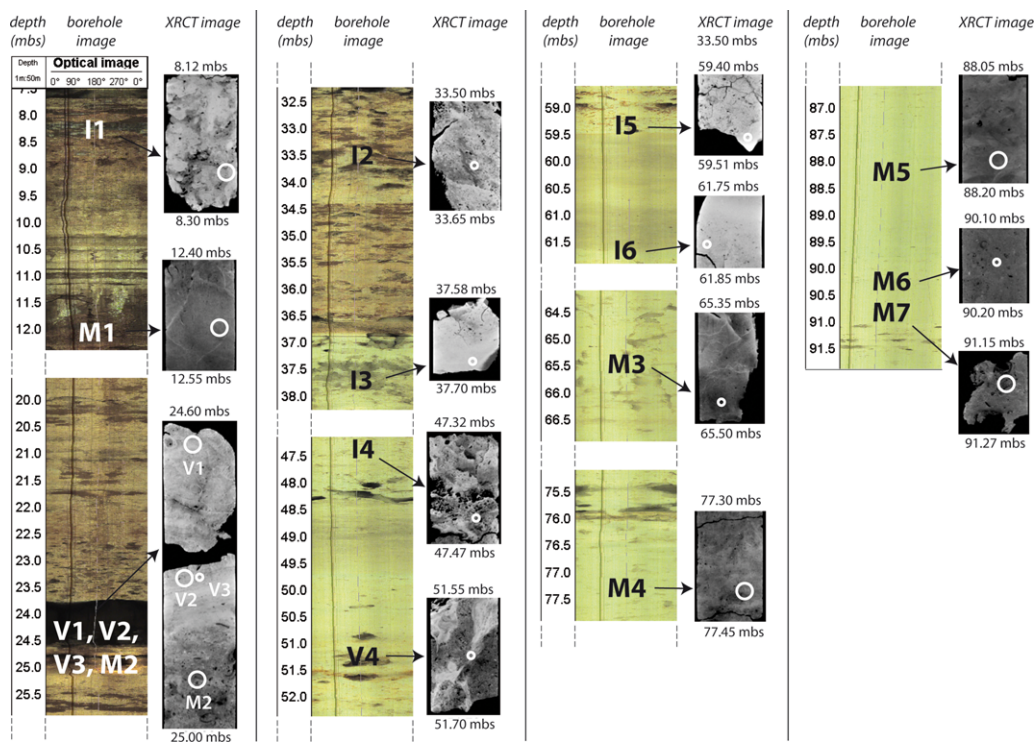


Fig. 2. Borehole images (continuously oriented 360° photography of the borehole wall) of MC10 and XRCT borehole core images between 7.0 and 92.0 mbs (from left to right) showing the reservoir heterogeneity. The location of miniplugs and microplugs are indicated on the borehole wall images and on the XRCT borehole core images.

MULTI-SCALE X-RAY TOMOGRAPHY ANALYSIS

Table 1. List of the XRMT images of the miniplugs and microplugs

Plug	Depth (mbs)	Geological unit	Lithofacies and subtypes	Sample size	Voxel size (μm)
M1	12.3	Inner platform	Ooidal grainstone	Miniplug	5.06
M2	24.9	Reef barrier	Peloidal wackestone	Miniplug	5.06
M3	65.5	Forereef	Skeletal grainstone	Microplug	1.75/0.7
M4	77.4	Forereef	Fine-grained skeletal packstone	Miniplug	5.06
M5	88.2	Forereef	Bioturbated and bioclastic packstone	Miniplug	5.06
M6	90.2	Forereef	Skeletal grainstone	Microplug	1.75/0.7
M7	91.0	Forereef	Skeletal grainstone/rudstone	Miniplug	5.06
V1	24.6	Inner platform	Partially dolomitized microbial wackestone	Miniplug	5.06
V2	24.7	Reef barrier	Partially dolomitized wackestone	Miniplug	5.06
V3	24.8	Reef barrier	Partially dolomitized wackestone	Microplug	2.12/1.06/0.42
V4	51.3	Reef barrier	Rudstone indurate by algal mats	Microplug	1.75/0.7
I1	8.2	Inner platform	Indurate mudstone	Miniplug	5.06
I2	33.5	Reef barrier	Coral boundstone	Microplug	1.75/0.7
I3	37.7	Reef barrier	Dolomitized algal wackestone	Microplug	2.12/1.06/0.42
I4	47.4	Reef barrier	Dolomitized rudstone	Miniplug	1.75/0.7
I5	59.5	Reef barrier	Framestone with mineralization	Microplug	2.12/1.06/0.42
I6	61.8	Forereef	Wackestone with dolomite crystals	Microplug	2.12/1.06/0.42

Synthesis of the type of plugs (miniplugs and microplugs) available for each sample and the corresponding voxel size, together with a geological description. For each sample listed in the table, there are also imaged macroplugs available (voxel size of 190 μm).

XRCT

X-ray tomography is a non-destructive imaging technique that generates a 3D volume of the sample from a set of 2D X-ray attenuation images. The monochromatic and parallel X-ray beam is attenuated by the components of the sample, and its refractive intensity is captured by a charged-coupled device (CCD) camera. Each of the camera pixels records the mean X-ray absorption value of the component. The 3D image reliability and precision increase as the voxel size and investigated volume decreases.

For a given porous media, the X-ray energy attenuation depends on solid-phase composition and porosity. The images are usually displayed in normalized grey levels, where a black colour represents the voids, white represents the rock matrix, and the greyscale levels denote micro-porosity and/or variations in grain density.

XRCT data acquisition and processing. The borehole core recovered from hole MC10 and the macroplugs were imaged using a helical XRCT scanner (General Electrics LightSpeed) at the Total Centre Scientifique et Technique Jean Feger (CSTJF), Pau, France. A total of 1600 radiographs were recorded over 360° using an exposure time of 0.35 s and an energy of 140 keV. The voxel size is 190 μm , hereafter referred to as 'low resolution', and the investigated volume of the macroplug is about

75 000 mm^3 . A calibration relating the X-ray density of the imaged macroplug and the experimental porosity measured on the same macroplug was performed so that the porosity of any macroplug can be derived from its X-ray density (Hebert 2011). Using the Avizo software tools developed by FEI Visualization Sciences Group virtual macroplugs were then extracted from the XRCT imaged borehole core of hole MC10 exactly where the miniplugs and microplugs were cored. The porosity of these virtual macroplugs was calculated using the calibrated relationship.

XRMT data acquisition. The miniplugs and microplugs were imaged at the ID19 beamline of the European Synchrotron Radiation Facility (ESRF), Grenoble, France. All of the plugs were investigated with voxel sizes ranging from 0.42 to 5.06 μm . The miniplugs were scanned along a length of 8 mm and with a voxel size of 5.06 μm , hereafter referred to as 'medium resolution'. The microplugs were imaged with the following combinations of voxel size: either 2.12, 1.06 and 0.42 μm or 1.75 and 0.70 μm , hereafter referred to as 'high resolution' (Table 1). The microplugs were scanned along a length ranging from 0.8 to 2.7 mm, depending on the resolution (0.42–2.12 μm side voxel). Both medium- and high-resolution acquisitions were made using a FReLoN CDD camera with 2048 \times 2048 pixels. A total of 2999 radiographs were recorded every 0.06° angle using either an exposure

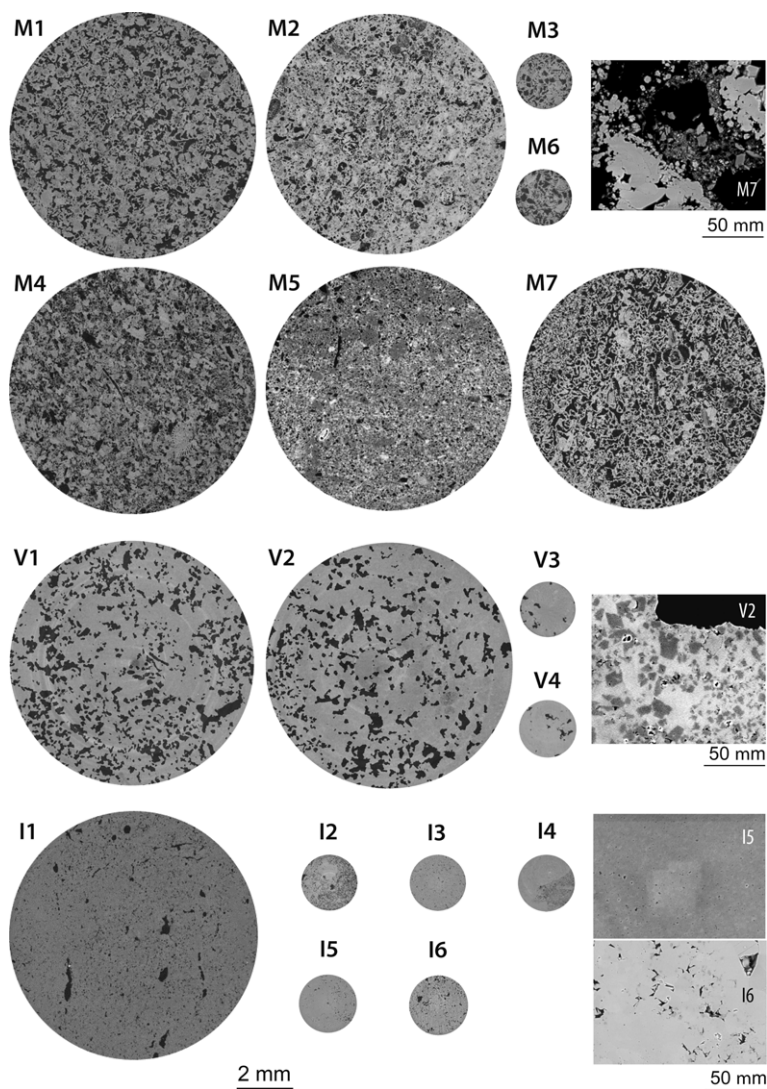


Fig. 3. Example of numerically computed cross-sections through the 3D XRMT images for all miniplugs and microplugs, and for one thin section SEM image of porosity groups M (moldic samples), V (vuggy samples) and I (intergranular micro-porous samples).

time of 0.5 s and 40 keV of energy for the medium-resolution acquisition, or 0.035 s and 13.6 keV (respectively) at high resolution.

The multi-resolution procedure supplies several XRMT images of the same sample with different voxel sizes and sampling volumes. For the medium resolution (i.e. voxel size of $5.06 \mu\text{m}$), the image volume is about 1000 mm^3 . For the high resolution, the sample volumes range from 0.4 to 6.2 mm^3 (with voxel sizes from 0.42 to 2.12, respectively). The high-resolution acquisition was

carried out at either scale using indirect detector microscopes for hard micro-imaging developed by Optique Peter (Lentilly, France). The system is composed of interchangeable eyepieces of different magnification that can be set up without removing the core sample from the beam axis (Douissard *et al.* 2012).

XRMT data processing. The 3D XRMT images of the rock sample are reconstructed by using the filtered back-projection algorithm implemented in

MULTI-SCALE X-RAY TOMOGRAPHY ANALYSIS

the High Speed Tomography in python version (PyHST) software package developed at the ESRF (Mirone *et al.* 2013).

The first step is to discriminate whether a voxel belongs to the rock matrix or void space for each of the images. We consequently applied first a median filter, and then segmented the images using the iterative growing-region segmentation described in Noiriél *et al.* (2005). Two threshold values are chosen to separate voids from solid rock, leaving a third region in-between that contains voxels that could either be voids or solid rock. The algorithm investigates the neighbouring voxels of the initial point and determines whether or not they should be added to the region. For the X-ray attenuation histograms of the miniplugs and microplugs (Fig. 4), the thresholds were chosen as the upper bound of the pore phase and the lower bound of the solid phase listed in Table 2 (miniplugs) and Table 3 (microplugs). The attenuation histograms of the vuggy (V1–V4) and micro-porous (I1–I6) samples show well-separated peaks characterizing the pore phase and the mineral phase. Hence, the identification can be performed

straightforwardly, although the void phase peak is less marked on the full-image histogram for the low-porosity samples. The attenuation histograms of the moldic samples (M1–M7) show an intermediate attenuation range between the pore and solid peaks that could be associated with the micro-porous phase (solid matrix with pores of a size smaller than the voxel size), as identified on SEM analysis of adjacent thin sections (Fig. 3). For the miniplugs, the micro-porous phase denotes material containing pores smaller than $5.06\ \mu\text{m}$. It corresponds to material containing pores smaller than 1.75 or $2.12\ \mu\text{m}$ for the microplugs imaged with the lowest resolution and pores smaller than 0.42 or $0.7\ \mu\text{m}$ for the microplugs imaged with the highest resolution. A three-phase (solid, void and micro-porous) segmentation procedure is *a priori* appropriate for samples displaying such attenuation histograms. However, this type of segmentation requires high-quality data and iterative procedures in comparison with measured porosity for obtaining reliable results (Garing *et al.* 2013b; Mangane *et al.* 2013). As the objective of this study is to identify the porosity that can be unambiguously assigned at a

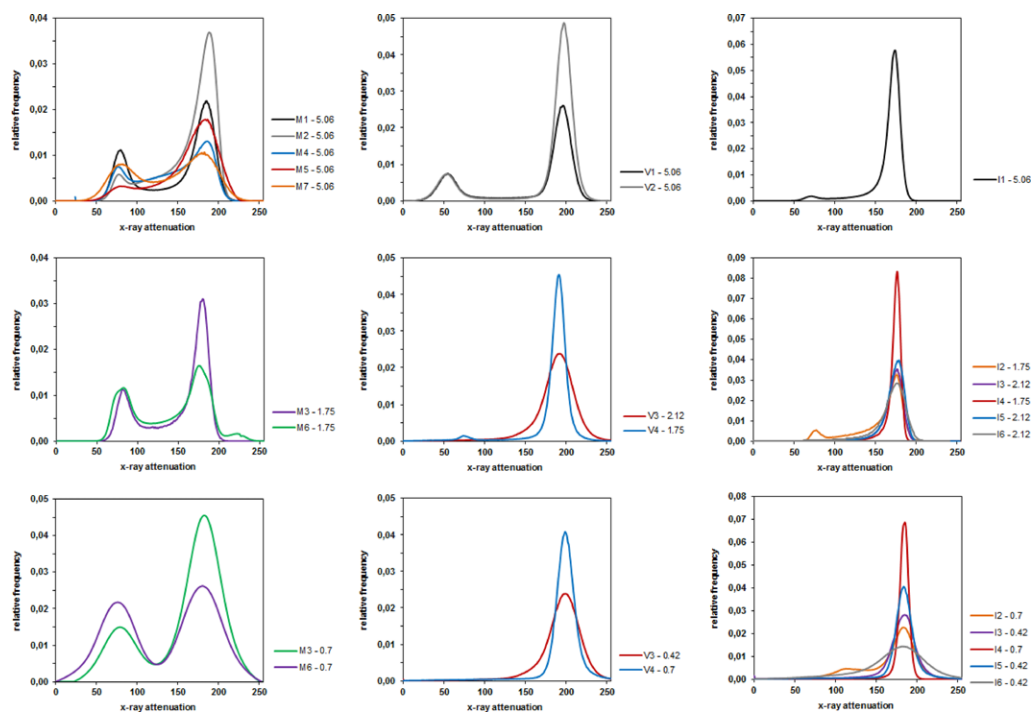


Fig. 4. X-ray attenuation histograms of the miniplugs and microplugs listed in Table 1, based on their pore type from the left-hand to the right-hand column (M for moldic samples, V for vuggy, and I for intergranular micro-porous), and the resolution of the images from top to bottom (5.09 mm for the miniplugs; 2.12 or 1.75 mm for the microplugs imaged with the lowest resolution; and 0.42 or 0.7 mm for the microplugs imaged with the highest resolution).

Table 2. *XRMT analysis of the miniplugs*

Plug	Segmentation thresholds	$\phi_{XRMT}^{(MR)}$ (%)	Connected pore network		ϕ_{XRCT} (%)	ϕ_{He} (%)	d_{DOM} (μm)
			No.	%/sample			
M1	103–137	29.6	1	96.7	43.7	50.4	
M2	99–109	31.4		–	22.3	0.7	
		macro: 12.0 micro: 19.4	macro: 0 macro + micro: 1	94.7			macro: 50 micro: 16
M4	108–136	29.6	1	97.0	45.1	45.6	53
M5	113–126	7.0	0	–	49.0	43.9	25
M7	97–115	40.4	1	95.5	48.3	45.6	57
V1	108–125	16.9	1	86.7	18.4	0.7	78
V2	83–112	18.2	1	82.0	24.2	0.7	84
I1	138–153	8.6	0	–	25.7	17.6	124

Results of porosity values ($\phi_{XRMT}^{(MR)}$) and connectivity (number of percolating clusters presented by the plug, and the proportion of the percolating cluster(s), in case there is one or more) of the miniplugs. The segmentation thresholds used as input in the region-growing algorithm are listed for each plug. The values of porosity computed on the corresponding virtual macroplug (ϕ_{XRCT}) and measured in laboratory on the nearest macroplug (ϕ_{He}) are also displayed in the table, as well as the dominant pore diameter (d_{DOM}).

given resolution and rock type in order to compare the accessible porosity depending on the resolution and the size of the imaged sample, all of the images are segmented into two phases. The study

of the micro-porous phase is performed by comparing images at different resolutions: micro-pores at 5.06 μm may become macro-pores at 0.42 μm . Nevertheless, one moldic miniplug (M2) was

Table 3. *XRMT analysis of the microplugs*

Plug	Voxel size (μm)	Segmentation Thresholds	$\phi_{XRMT}^{(MR)}$ (%)	Connected pore network		ϕ_{XRCT} (%)	ϕ_{He} (%)	d_{DOM} (μm)
				No.	%/sample			
M3	1.75	139–149	32.1	1	95.7	39.9	48	
	0.7	126–157	30.3	1	96.6			
M6	1.75	140–151	41.3	1	98.7	48.1	45.6	47
	0.7	131–159	45.1	1	99.1			31
V3	2.12	156–174	2.7	0	–	22.3	0.7	
	1.06	150–164	6.7	0	–			
	0.42	148–165	14.9	1	14.2			4
V4	1.75	139–171	4.3	0	–	29.1	47	40
	0.7	139–172	5.2	2	16.3–36.3			35
I2	1.75	170–180	23.9	1	70	27.2	27	
	0.7	156–169	24.8	1	78			
I3	2.12	119–135	2.1	0	–	10.1	40	
	1.06	131–151	5.2	0	–			
	0.42	133–157	5.3	0	–			
I4	1.75	178–191	4.6	1	65	35.9	31	7.5
	0.7	133–147	3.5	1	80			2.1
I5	2.12	155–170	2.7	0	–	14.9	19	8
	1.06	152–172	3.0	Na	Na			
	0.42	158–167	5.0	Na	Na			2.1
I6	2.12	143–157	9.1	1	72.2	12.6	28	24
	1.06	144–160	11.6	0	–			
	0.42	147–162	14.3	1	86.1			15

Results of porosity values ($\phi_{XRMT}^{(MR)}$) and connectivity (number of percolating clusters presented by the plug, and the proportion of the percolating cluster(s), in case there is one or more) of the microplugs for each resolution. The segmentation thresholds used as input in the region growing algorithm are listed for each plug. The values of porosity computed on the corresponding virtual macroplug (ϕ_{XRCT}) and measured in laboratory on the nearest macroplug (ϕ_{He}) are also displayed in the table, as well as the dominant pore diameter (d_{DOM}).

MULTI-SCALE X-RAY TOMOGRAPHY ANALYSIS

segmented into three phases for comparison. The three-phase segmentation methodology is further detailed in Garing *et al.* (2013b).

Once the pore phase has been identified, the pore-size distribution can be investigated. The pore-size distribution function gives the probability that a random point in the pore phase lies at a given distance from the nearest point onto the pore–solid interface (Coker & Torquato 1995). It is achieved for each ‘point’ (voxel) of the pore phase by finding the largest sphere centred on the point that just touches the pore phase and by recording its radius (Euclidean distance between the point of interest and the one on the pore–solid interface). The spheres that are fully included in larger ones are not considered. The algorithm used is a modified version of the one described in Meijster *et al.* (2000). In the latter, d_{DOM} refers to the pore diameter corresponding to 50% porosity contribution (i.e. the maximum size of pores needed to occupy half of the pore space). This value is considered as the dominant pore diameter of the sample.

The porosity computed from the segmented images corresponds to the total porosity of the samples. However, the connected porosity can be estimated by identifying the network of pore voxels corresponding to the pores. The connected pore networks that are also connected to the two physical boundaries of the sample are referred to as percolating clusters. To achieve this distinction between connected and isolated pore networks, we used the cluster-labelling algorithm described by Stauffer & Aharony (1994).

The total porosity was computed for each mini-plug and for each microplug at different resolutions.

The pore-size and connectivity analysis were conducted for most of the miniplugs and microplugs.

Results

Macroplugs

The porosity and permeability values measured for the 40 mm-diameter macroplugs are presented in Figure 5a, b. The measured porosity is referred to as ‘experimental porosity’ by determining the change in helium pressure, and named ϕ_{He} . As expected, the measurements highlight the heterogeneity of the reservoir; the porosity values range from very little to 50.5%, with a mean value of 36.5%. The permeability values range from almost 0.0 to 20.4 mD, with the mean of the dataset centred around 800 mD. The overall $k - \phi$ dataset exhibits a distinct correlation between porosity and permeability (Fig. 5c); the $k - \phi$ trends include low porous–low permeable, low porous–high permeable, high porous–low permeable and high porous–highly permeable rocks. There is also no particular correlation within groups of data organized according to geological units, lithofacies or pore type. For instance, the porosity values of the two macroplugs cored adjacent to the moldic mini-plugs M4 and M7 are similar; however, the permeability values differ by more than one order of magnitude.

The porosity values calculated from the XRCT images of the macroplugs, named ϕ_{XRCT} , are presented as a function of depth in Figure 5a, together with the experimentally determined porosity. The values range from 18.2 to 56.8%, with a mean value of 40.7%. The XRCT porosity values are

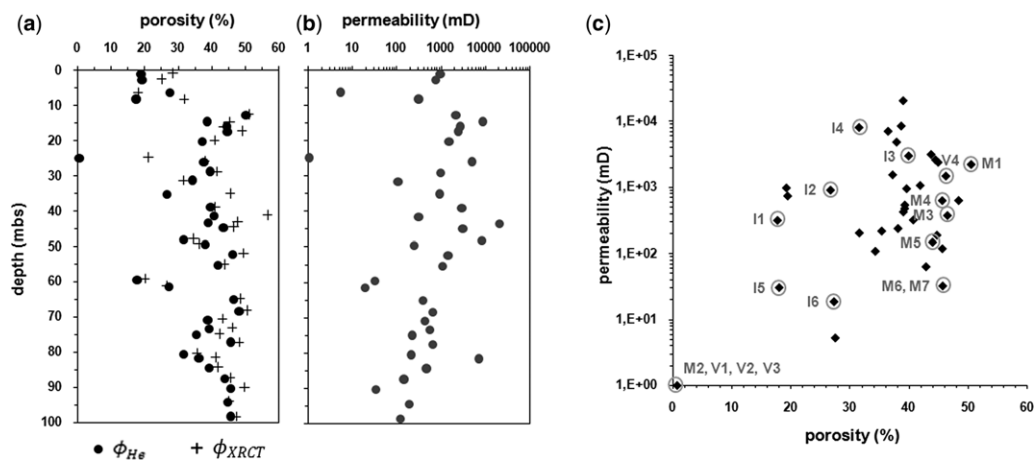


Fig. 5. Porosity and permeability for the macroplugs. (a) Experimental porosity (ϕ_{He}) and computed porosity ϕ_{XRCT} v. depth; (b) permeability v. depth; (c) $k - \phi$ cross-plot.

close to the experimental values, with some discrepancies observed for the inner platform unit (from 0 to 25 mbs) and the karstified barrier reef unit (from 25 to 61.7 mbs). The computed porosity is close to, but still higher than, the measured porosity. The values of ϕ_{XRCT} listed in Tables 2 and 3 correspond to the porosity calculated on the virtual macroplugs extracted from the XRCT imaged borehole core where a real miniplug or microplug was cored, as explained in the XRCT data-processing section. Since the porosity of the virtual macroplugs is estimated from an experimentally determined calibration curve (see above), we consider these values of ϕ_{XRCT} to be more representative of the porosity at the location of the miniplugs and microplugs compared to the experimentally determined porosity ϕ_{He} measured on a macroplug that was cored nearby.

Miniplugs. The porosity values computed from the analysis of the XRMT images of the 9 mm-diameter miniplugs (voxel size of 5.06 μm), named $\phi_{\text{XRMT}}^{(\text{MR})}$, are lower than ϕ_{XRCT} and ϕ_{He} , especially in the case of samples M5 and I1 (Table 2). Samples V1, V2 and M2 were cored in a particularly heterogeneous diagenetic zone studied in great detail by Garing *et al.* (2013b) and located near 25 mbs. The macroplug was sampled in the tightest level with a very-low-porosity value (0.7%) that is not representative of the entire zone, and cannot be compared to the values computed for samples V1, V2 (V3) and M2. The porosity of miniplugs V2 and M2 was measured in the laboratory by Garing *et al.* (2013b) as 14.9% for V2 and 30.1% for M2. Also, sample M2 was segmented into three phases: void, micro-porous phase and solid phase. Percolating clusters were found for all of the samples except M5 and I1, which are the miniplugs presenting the lowest values of $\phi_{\text{XRMT}}^{(\text{MR})}$. The analysis of M2 using the three-phase segmentation shows that no percolating cluster can be found when only macro-pores are considered. However, a combination of the macro-pores and the micro-porous phase forms a well-connected network. The pore-size distribution functions ($P(x)$) are plotted in logarithmic scale (Fig. 6a, c & e) and in terms of volume fraction ($P(x)V(x)$) where $V(x)$ is the volume of a sphere of diameter x : Fig. 6b, d & f). For the miniplugs, results are available for samples M2, M4, M5 and M7 (Fig. 6a & b), samples V1 and V2 (Fig. 6c & d) and samples I1 (Fig. 6d & e). Samples V1 and V2 exhibit similar pore-size distributions, with a dominant pore diameter, d_{DOM} , close to 80 μm (Table 2). The dominant pore sizes of the moldic samples are smaller, in particular for sample M5: samples M7, M4 and M5 have d_{DOM} values of 57, 53 and 25 μm , respectively, while the dominant pore diameter of sample

M2 is 50 μm for the macro-pores and 16 μm for the micro-porous phase. Surprisingly, sample I1 is the microplug with the highest d_{DOM} (around 120 mm). This is due to the presence of a large macro-pore in the miniplug. The low value of porosity computed for sample I1 compared to the experimental value suggests a large amount of small size pores (below resolution).

Microplugs

Cross-sections computed numerically from the 3D images of three 2 mm-diameter microplugs (V3, I3 and I6) at voxel sizes of 2.12, 1.06 and 0.42 μm , respectively (Fig. 7), show that micro-porosity, which could not be seen with larger voxel sizes, can now be identified with our best resolution (voxel size of 0.42 μm). This is particularly straightforward for sample V3, where the matrix appears micro-porous at a voxel size of 0.42 μm , whereas it appears as solid rock at a voxel size of 2.12 μm and for the nearby miniplug V2 imaged with a voxel size of 5.06 μm (Fig. 3).

The porosity profiles (porosity values along the sample length) computed from sample I5 images acquired with the three different voxel sizes of 2.12, 1.06 and 0.42 μm , respectively, can be compared and provide a quantitative example of the XRMT multi-resolution analysis (Fig. 8a). Recall that the images with voxel sizes of 2.12 and 1.06 μm consider the same 2 mm-diameter area, while the image with a voxel size of 0.42 μm investigates only a 0.8 mm-diameter area within the 2 mm-diameter images. The porosity profiles are presented for the sample length shared by the three images. The porosity profiles computed for the images with a voxel size of 2.12 and 1.06 μm show a similar trend and order of magnitude, whereas the porosity profile computed from the image with a voxel size of 0.42 μm displays a similar trend but with higher porosity values. In order to investigate the same object, a subsample corresponding to the volume imaged by the smallest voxel size (0.42 μm) is extracted from the image with the highest voxel size (2.12 μm). The porosity profiles computed for this subsample and that from the image obtained with a voxel size of 0.42 μm are similar for part of the sample only (Fig. 8b).

The values of the porosity computed for the microplugs, named $\phi_{\text{XRMT}}^{(\text{HR})}$, are detailed for each voxel size used (2.12, 1.06 and 0.42 μm ; 1.75 and 0.7 μm) and either lower than the porosity values measured on the nearest macroplugs (ϕ_{He}) located nearby, or that of porosities calculated for the virtual macroplugs (ϕ_{XRCT} : Table 3). This difference is particularly visible for the vuggy samples (V3, V4) and most of the micro-porous samples (I3, I4, I5, I6). It appears that the porosity values

MULTI-SCALE X-RAY TOMOGRAPHY ANALYSIS

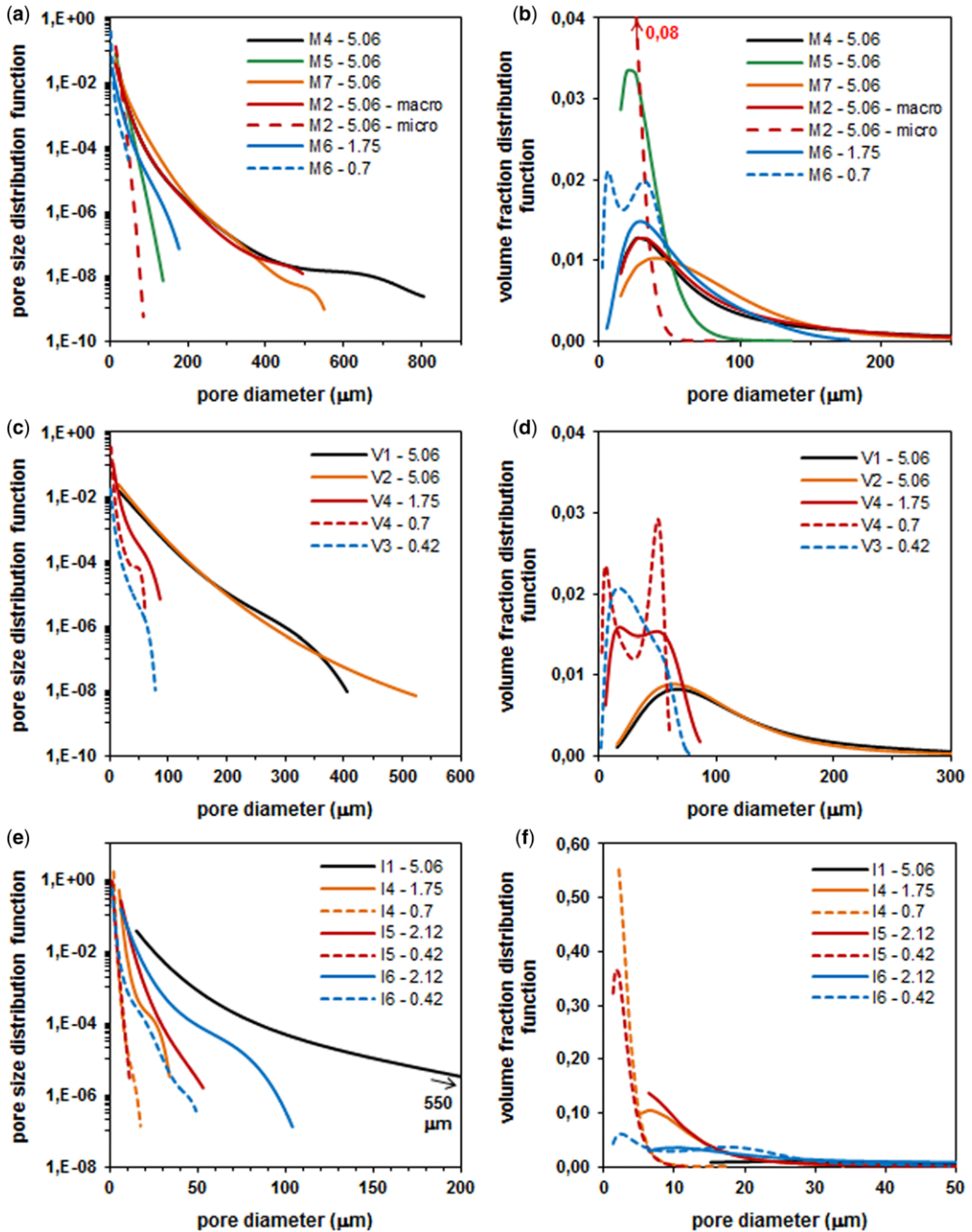


Fig. 6. Normalised probability density functions (PDF) expressing the pore-size distribution (a, c and e) and the corresponding porosity volume fraction distribution (b, d and f) for moldic samples (a, b); vuggy samples (c, d); and intergranular micro-porous samples (e, f). The peaks in graphs b, d and f correspond to the dominant pore size of the sample.

computed for these microplugs depend on the resolution to a greater extent than moldic microplugs. In the case of moldic samples (M3, M6)

and sample I2, the values of $\phi_{\text{XRMT}}^{(\text{HR})}$ are closer to the values of ϕ_{XRCT} and ϕ_{He} . These values are also similar when they are computed for the

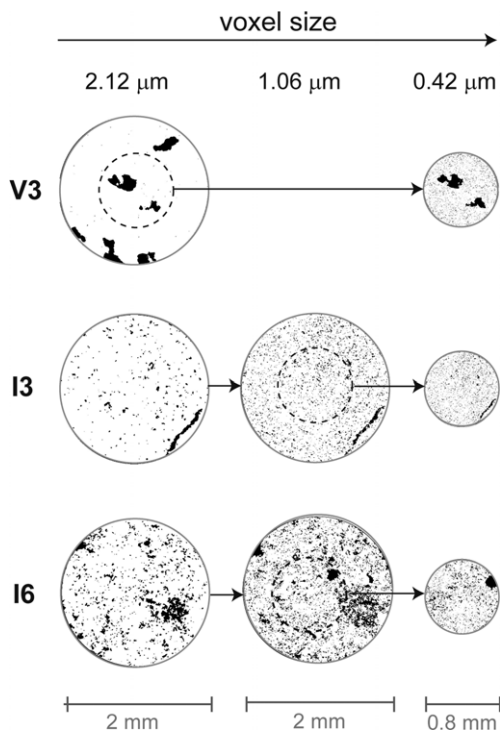


Fig. 7. Example of numerically computed cross-sections through the segmented 3D XRMT images of three microplugs (V3, I3 and I6) with voxel sizes of 2.12, 1.06 and 0.42 μm , respectively. The images in the first two columns of V3, I3 and I6 represent the same 2 mm-diameter area, whereas the images in the right-hand column represent a 0.8 mm-diameter area, centred in the 2 mm-diameter area investigated with the lower resolutions.

images with the voxel size of 1.75 and of 0.7 μm . In addition, the percolating cluster analysis shows that the pores identified at both resolutions form a well-connected network. Percolating clusters are also found at the lowest and highest resolution for samples I4 and I6. We note that the connectivity increases with the resolution for all of these samples (M3, M6, I2, I4 and I6). In the case of the vuggy microplugs (V3, V4), percolating clusters are only found at the highest resolution (voxel size of 0.42 μm). The identified connected pore networks represent a small percentage of the total porosity. Finally, no percolating clusters were found for samples I3 and I5. A pore-size distribution analysis is available for sample M6 (Fig. 6a & b), samples V3 and V4 (Fig. 6c & d), and samples I4, I5 and I6 (Fig. 6e & f). The smallest pore diameters investigated for the images with voxel sizes of 2.12 μm , 1.75 μm , 0.7 mm and 0.42 μm are 6.36, 5.25, 2.1 and 1.26 μm , respectively. For all samples, the

pore network identified at the highest resolution exhibits a larger amount of small pores. Sample M6 has a dominant pore diameter, d_{DOM} , of 47 μm when imaged with a voxel size of 1.75, and 31 μm when imaged with a voxel size of 0.7 μm (Table 3). These values of d_{DOM} are far above the size of the smallest identified diameter and are actually higher than for sample M5 imaged with a voxel size of 5.06 μm . Sample V4 has a similar d_{DOM} of 40 μm (voxel size of 1.75 μm) and 35 μm (voxel size of 0.7 μm). However, sample V3 has a smaller d_{DOM} of 4 μm (voxel size of 0.42 μm). In the case of samples I4 and I5, the dominant pore size is very close to the size of the smallest visible pores: for sample I4, d_{DOM} is equal to 7.5 μm (voxel size of 1.75 μm) and 2.12 μm (voxel size of 0.7 μm), and for sample I5, d_{DOM} is equal to 8 μm (voxel size of 2.12 μm) and 2.15 μm (voxel size of 0.42 μm). Sample I6 has larger d_{DOM} values of 24 μm (voxel size of 2.12 μm) and 15 μm (voxel size of 0.42 μm).

In summary, the overall porosity values obtained for the macroplugs, miniplugs and microplugs can be plotted by depth together with the geological units and borehole image from hole MC10 (Fig. 9), as well as in 2D sections of the pore structure investigated for plugs V2, V3, I4 and I6 at a voxel size of 190 μm (virtual macroplug), 5.09 μm or close to 2 μm (miniplug or microplug at the lowest resolution) and smaller than 1 μm (microplug with the highest resolution).

Discussion

Spatial variability of the porosity

The overall dataset highlights the spatial variability, hence heterogeneity, of the pore structure, especially in the inner platform and reef barrier units that correspond to a palaeo-karstic environment with alternating cemented layers and large dissolution features (channels and vugs). The samples cored in these geological units, which include a wide range of heterogeneous structures even at a small scale, display distinct porosity features depending on size and core location (Fig. 9). The spatial variability of the porosity in these zones is already visible at the macroplug scale. The values of porosity measured from a macroplug (ϕ_{He}) and computed from the extracted pore structure of a macroplug located nearby (ϕ_{XRCT}) always differ for the inner platform and reef barrier samples, whereas they are usually similar for the forereef samples (Tables 2 and 3). It is hence difficult to compare the characterization of the pore network from the XRMT images of the miniplugs and microplugs with the measured porosity/permeability values of nearby macroplugs.

MULTI-SCALE X-RAY TOMOGRAPHY ANALYSIS

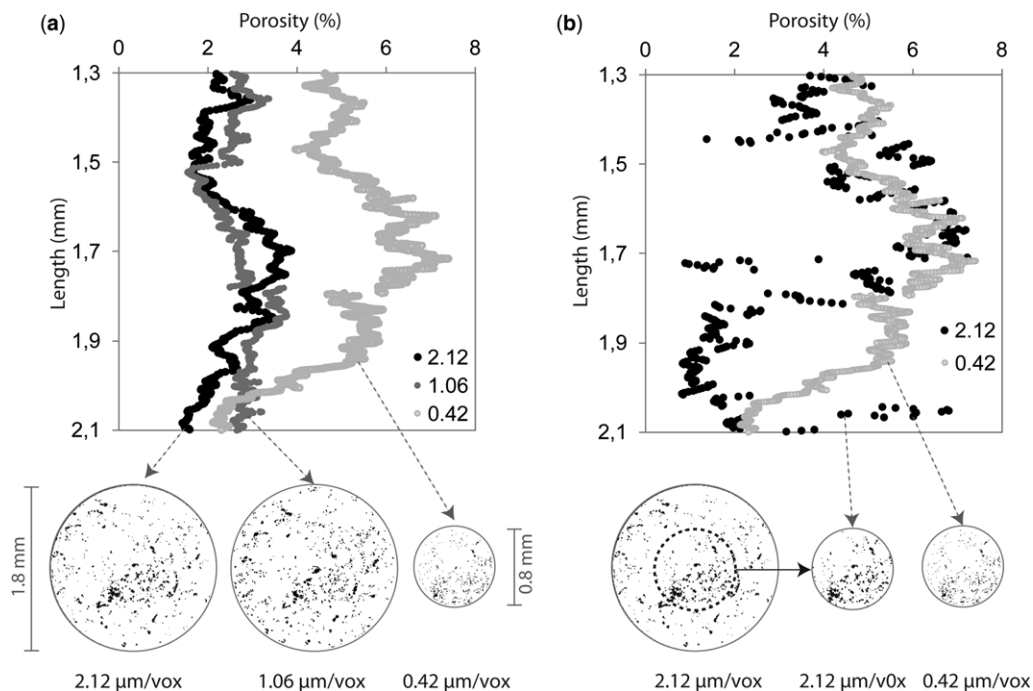


Fig. 8. Porosity profiles computed for microplug I5: (a) at voxel sizes of 2.12, 1.06 and 0.42 μm (note that the right-hand image represents a smaller volume) and (b) at voxel sizes of 2.12 and 0.42 μm (this time the same sample volume remains the same).

The effect of sampling is even more important when smaller samples, for example, miniplugs or microplugs, are extracted from the zones that display significant heterogeneities, such as that visible from borehole wall images. For example, the XRCT image of the borehole core where miniplug I1 was cored (Fig. 2) contains centimetre-scale pore structures (e.g. vugs) that are not sampled by I1 but could be sampled by a macroplug. We further note that the value of porosity computed for I1 ($\phi_{\text{XRMT}}^{(\text{MR})}$) is a third of the value computed from the corresponding virtual macroplug (ϕ_{XRCT}). However, for the miniplugs and microplugs, the porosity estimation depends on the image resolution and the segmentation process, as detailed in the next subsection.

Effect of resolution on porosity

A critical issue related to the precise quantification of porosity from XRMT images is the representativeness of data, which depends on the contrast between the investigated volume, the image resolution and the size of the pore network. This issue is discussed individually in the following for the three rock types.

Vuggy samples. The results of the XRMT analysis of samples V2 and V3 (i.e. a miniplug and a microplug imaged with three voxel sizes and cored adjacent to each other) highlight the effect of resolution on porosity estimation. The connected porosity computed using sample V2 (voxel size of 5.06 μm) is in good agreement with the experimentally determined porosity value of 14.9% reported by Garing *et al.* (2013b). The authors also conducted mercury injection tests on sample V2 and reported a mean throat diameter of 45 μm , which is larger than the image resolution. The value of porosity computed using the smaller sample (i.e. microplug V3) differs from the experimental measurement. The porosity value estimated from the image at the highest resolution (voxel size of 0.42 μm) is identical to the experimentally determined porosity of 14.9%. However, only 14.2% of the identified porosity forms a connected network, leading to an overall computed connected porosity of 2.1%, which is much smaller than the experimental value. Also, the dominant pore size of sample V3 imaged with the smallest resolution is a tenth of the throat size estimated using mercury injection. Microplug V3 (voxel size 0.42 μm) comprises of a micro-porous matrix with a small fraction

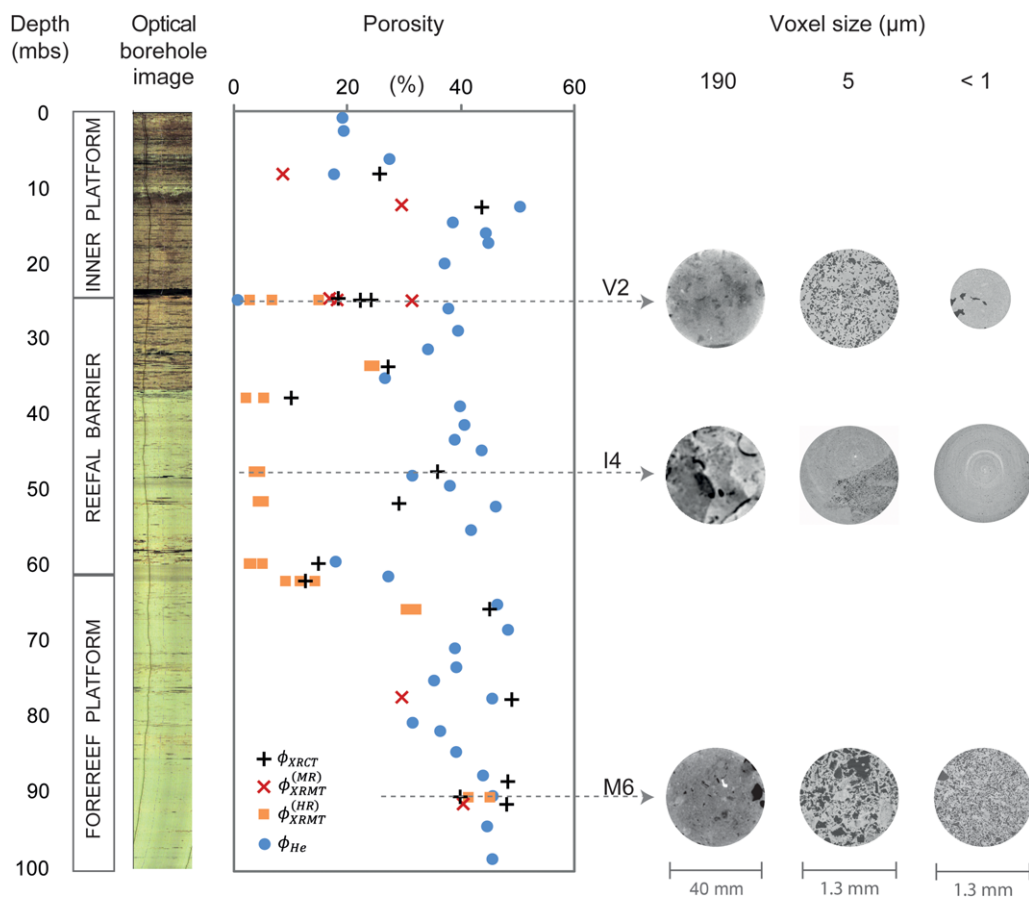


Fig. 9. Values of porosity measured in laboratory (ϕ_{He}), porosity computed for the XRCT images of the macroplugs (ϕ_{XRCT}), porosity computed for the XRMT images of the miniplugs at medium resolution ($\phi_{XRMT}^{(MR)}$) and of the microplugs at high resolution ($\phi_{XRMT}^{(HR)}$), plotted as a function of the depth. Three examples of the pore structure investigated on virtual macroplugs (voxel size of 190 μm), corresponding miniplugs or microplugs imaged with a voxel size around 2 μm and corresponding microplugs imaged with a voxel size smaller than 1 μm are displayed for samples V2-V3, I4 and M6 on the right of the graph. The geological units as well as the borehole image are also displayed on the left of the graph.

of randomly localized vugs, while a tight matrix with homogeneously dispatched vugs is identified with miniplug V2 (Fig. 7). However, as the smallest pores have almost no contribution to the overall porosity, the highest resolution is not suitable for porosity estimation of such a rock type. The images of microplug V3 (voxel sizes of 2.12 and 1.06 μm) are also not appropriate as they cannot be used to correctly evaluate the distribution of vugs, mostly due to the limited size of the sample (Fig. 4). For this type of carbonate, XRMT analysis at high resolution, requiring an image to be made from a small rock sample, is not recommended as major heterogeneities present at larger scales cannot be captured.

Moldic samples. The moldic samples imaged with a voxel size of 5.06 μm display a large number of pores that are clearly identifiable with this fairly low resolution but also show a considerable number of pores with a size below 5.06 μm that cannot be identified, and are therefore not included in the void phase. The presence of a significant microporous phase can be inferred from the attenuation histograms (Fig. 4), SEM analysis of thin sections (example of sample M7: Fig. 3) and mercury injection tests conducted on sample M2, giving a mean throat diameter of 3.9 μm (i.e. smaller than the XRMT image resolution). The low-porosity values computed for the miniplugs compared to that computed from the corresponding macroplugs indicate

MULTI-SCALE X-RAY TOMOGRAPHY ANALYSIS

the presence of micro-porosity, which cannot be identified using a two-phase segmentation.

The segmentation of XRMT images from sample M2 into three phases here provides a means to quantify the micro-porosity. The computed connected porosity value is in good agreement with the experimental porosity measurement conducted on the same sample by Garing *et al.* (2013*b*). It appears that three-phase segmentation is necessary to obtain an accurate estimate of porosity for this type of moldic carbonate. However, the connectivity of the micro-pores within the micro-porous phase cannot be directly measured. Instead, it requires the analysis of subvolumes at higher resolution. Moreover, without any information about the geometry of the pore network forming the micro-porous phase, it is necessary to assume a value of percolation threshold above which the micro-pores are fully connected and hence become permeable. To the best of our knowledge, there are very few published data concerning the value of the percolation threshold for carbonates. Luquot & Gouze (2009) evaluated the porosity value at the percolation threshold ($\phi_c = 0.059$) of an oolitic carbonate from precipitation experiments, while the percolation threshold of polydisperse sphere assemblage is close to 0.030 (van der Marck 1996). The connectivity analysis of sample M2 shows that the macro-pores are only connected by the micro-porous phase, which is also probably the case of sample M5, for which no percolating cluster was found at medium resolution (voxel size of 5.06 μm). For this type of carbonate, the smallest pores, which are not imaged at medium resolution, contribute to at least half of the total porosity value and may, in some cases, also contribute to the overall connectivity of the pore network. In order to investigate the efficiency of high resolution (voxel sizes of 1.75 and 0.7 μm), we can compare the XRMT analysis results for samples M6 and M7 to a microplug and a miniplug sampled from the same zone. It should be noted that the moldic samples present more homogeneously distributed heterogeneities that are also of smaller size, unlike, for instance, the vuggy samples. As a result, the pore structures sampled by the 9 mm-diameter and the 2 mm-diameter plugs do not differ noticeably (Fig. 3). The pores identified from one of the microplugs (M6) display a smaller dominant diameter than the ones identified from the miniplug (M7). However, only pores larger than 5.06 μm are included in the image for M7, whereas M6, which was imaged at the highest resolution, includes pores with sizes ranging from 0.7 to 5.06 μm . The value of porosity computed from the image at highest resolution matches the experimentally determined porosity, and the identified pore network is almost entirely connected.

For moldic samples with molds of similar size or smaller than that presented in this dataset, the highest resolution images alone lead to a correct representation of the pore structure. However, for a sample that contains larger molds, the pore structure investigated by a microplug will probably not yield the correct global representation of the sample. Both medium- and high-resolution X-ray micro-tomography images therefore appear necessary to characterize such samples.

Intergranular micro-porous samples. The XRMT analysis of miniplug I1 imaged at medium resolution (voxel size of 5.06 μm) suggests the presence of much smaller micro-pores that might even be difficult to identify using a three-phase segmentation. The identification of these micro-pores is difficult because mudstones often have very small and evenly distributed micro-pores (Lonoy 2006). The porosity value computed for the miniplug is low in comparison to the experimentally determined porosity. In addition, the absence of connectivity for the identified pore network suggests that medium resolution is inappropriate to obtain a precise porosity estimate or to conduct further analysis of the pore structure of such a sample. Most of the microplugs were sampled in the reef barrier unit, which presents heterogeneities at all scales, including submillimetre to centimetre scales. Therefore the effect of the resolution on porosity characterization needs to account for the impact of sample size and sample location. The multi-resolution analysis of sample I5 indicates that the porosity computed for the image with a voxel size of 0.42 μm is nearly 2% higher than the porosity computed for the images with voxel sizes of 2.12 and 1.06 μm (Fig. 8a). This difference is not due only to the decreasing image volume linked to the increasing resolution: the porosity profiles from the bottom-most part of the plug illustrate how difficult it is to detect micro-pores smaller than 1 μm from the images with a voxel size of 2.12 μm (Fig. 8b). This difficulty leads to a systematic underestimation of porosity.

However, even if more pores are identified with the best resolution, the computed porosity value is still much lower than the experimental one. The SEM analysis and pore-size distribution of the sample suggest that the difference between the two porosity values is not due to sampling issues but caused by the presence of smaller micro-pores that cannot be identified, even at the highest resolution. This is also probably the case for samples I3 and I4.

Conversely, samples I2 and I6 display larger pores that can be identified from XRMT images. Hence, the porosity computed for these microplugs imaged with the highest resolution is close to the

value measured from the virtual macroplug. Recall that the nearest macroplug to sample I6 is cored from a different type of carbonate rock and hence should not be compared to microplug I6. Garing *et al.* (2013*b*) measured the porosity from a mini-plug cored aside microplug I6 and reported a value of 12.1%, which corresponds to the porosity computed for the virtual macroplug and to the connected porosity value computed for microplug I6 with a voxel size of 0.42 μm .

For all of these samples, the smallest pores contribute to at least half of the total porosity. Hence, microplugs imaged with the highest resolution are needed to obtain an accurate porosity estimate. However, for the less porous samples with very small pores, even the highest resolution will not provide a reliable representation of the pore network. Thus, XRMT images cannot be used to estimate the porosity of such samples. Any detailed porosity analysis would then require X-ray nanotomography to better image the micro-porosity and, of course, classical laboratory measurements and thin section analysis. In all cases, thin sections will still contain additional information and should be used as complementary data of XRMT images, as suggested by Remeysen & Swennen (2008).

Implications for transport properties and upscaling in reefal carbonates

This study illustrates that high-resolution XRMT techniques are helpful in investigating the 3D pore structure at the small scale, and provide an insight into the distribution and connectivity of micro-porosity that cannot be obtained from images with lower resolution. When using a low-resolution micro-CT scanner, the limitations of XRMT techniques appear such as the impact of artefacts enhanced by dual-energy techniques (Remeysen & Swennen 2008). In this study, the use of synchrotron CT with high resolution, which ranges from tens of nanometres to a few microns, together with monochromatic X-rays lead to the construction of high-quality and, therefore, more accurate images that provide a better quantification of the different carbonate phases. However, the results still highlight limitations inherent to X-ray CT techniques: small sample sizes that are required for high-resolution images can be non-representative if they are located in carbonates with significant macro-scale heterogeneity. In such cases, different sample locations will lead to different characterizations of the pore space and resulting petrophysical properties. Moreover, many carbonate rocks may present micro-porous material for which the details of the pore-space geometry cannot be resolved, even with the highest resolution used in this study (voxel size

of 0.42 μm) because pores even smaller than this resolution are present. A good example of these limitations is sample I4: at microplug scale, the carbonate rock of the zone where I4 was sampled appears to be of low porosity (close to 4%) and not well connected, although the macroplug cored in the exact same zone appears to have a high porosity (31%) and permeability (8.0 D), suggesting a well-connected pore network. The three-phase analysis of sample M2, and the multi-scale analysis of samples M6 and M7, confirm that the micro-porous phase often controls the connectivity of the sample and, hence, the flow properties of the rock (Dullien 1979; Clennell 1997; Gouze & Luquot 2011; Garing *et al.* 2013*b*). Even if this micro-porous phase can be identified from XRMT images, the inability to completely extract the network of the micro-pores contained in the phase limits the direct computation of transport properties from XRMT images, although new pore-network modelling techniques (Jiang *et al.* 2013*a, b*; Prodanović *et al.* 2014) may overcome this challenge in the near future. Similarly, the computation of other petrophysical properties remains elusive. Knackstedt *et al.* (2008) attempted to integrate the micro-porous phase in the computation of resistivity and acoustic properties using empirical and theoretical relationships but concluded that more information was needed to compute the petrophysical properties if rocks contain significant micro-porosity.

Conclusion

We investigated the heterogeneity of porosity from reefal carbonate rocks across multiple scales (from the pore to centimetre scale) using X-ray microtomography. Compared to standard direct measurements of porosity and permeability on core samples, the non-invasive 3D imaging of the pore structure provides an opportunity to relate the macroscopic properties (e.g. porosity and permeability) to the intrinsic variability and hierarchy of the connected pore space, which was caused by complex deposition and alteration processes over geological time. Limitations in terms of sampling size and resolution of the imaging tools remain a major difficulty for quantifying the relationship between pore structure, porosity and permeability in carbonate rocks. It is hence essential to develop multi-scale experimental approaches and to apply them to multiple samples to obtain statistically relevant results for petrophysical properties. This study shows that multi-scale XRMT imaging of multi-porosity carbonates is possible and manageable. This approach is complementary to standard laboratory measurements, and is essential for improving our

MULTI-SCALE X-RAY TOMOGRAPHY ANALYSIS

understanding of the origin of the large variability of porosity and permeability in carbonates. The relationship between porosity and (relative) permeability requires further analysis of the X-ray micro-tomography multi-resolution approach to (1) identify the optimal resolution required for measuring the controlling parameters (i.e. tortuosity, constrictively, connectivity) and (2) merge the data acquired at different scales. These investigations, coupled with pore-scale modelling, are in progress and will be presented in the future.

We wish to acknowledge the French National Centre of Scientific Research (CNRS) with H+, OREME, the Languedoc-Roussillon region, the European Community (EKV-2001-00039) and Total for financial support. We thank the Environmental Ministry of the Government of the Balearic Islands, in the persons of C. González Casanovas and A. Baron, for their support for the development of the experimental site at Ses Stijoles. We also thank E. Boller for her invaluable help in the data acquisition at the European Synchrotron Radiation Facility (ESRF, Grenoble) and O. Rodriguez (Voxaya, Montpellier) for help in processing the X-ray micro-tomography data.

References

- ARCHIE, G. E. 1952. Classification of carbonate reservoir rocks and petrophysical considerations. *American Association of Petroleum Geologists Bulletin*, **36**, 278–298.
- ARNS, C. H., KNACKSTEDT, M. A., PINCZEWSKI, W. V. & LINDQUIST, W. B. 2001. Accurate computation of transport properties from microtomographic images. *Geophysical Research Letters*, **28**, 3361–3364.
- ARNS, C. H., KNACKSTEDT, M. A., PINCZEWSKI, W. V. & MARTYS, N. 2004. Virtual permeametry on microtomographic images. *Journal of Petroleum Science and Engineering*, **45**, 41–46.
- ARNS, C. H., SAKELLARIOU, A., SENDEN, T. J., SHEPARD, A. P., SOK, R. M., PINCZEWSKI, W. V. & KNACKSTEDT, M. A. 2005. Digital core laboratory: petrophysical analysis from 3D images. *Petrophysics*, **46**, 260–277.
- BLUNT, M. J., BIJELJIC, B. ET AL. 2013. Pore-scale imaging and modeling. *Advances in Water Resources*, **51**, 197–216.
- BRUNAUER, S., EMMETT, P. H. & TELLER, E. 1938. Adsorption of gases in multimolecular layers. *Journal of American Chemical Society*, **60**, 309–319.
- CASTELEYN, L., ROBION, P., DAVID, C., COLLIN, P. Y., MENÉNDEZ, B., FERNANDES, N., DESAUBLIAUX, G. & RIGOLLET, C. 2010. An integrated study of the petrophysical properties of carbonate rocks from the 'Oolithe Blanche' formation in the Paris Basin. In: BAUD, P. & SCHUBEL, A. (eds) *Thermo-Hydro-Chemo-Mechanical Couplings in Rock Physics and Rock Mechanics. Tectonophysics*, **503**, 18–33, <http://dx.doi.org/10.1016/j.tecto.2010.09.031>
- CHOQUETTE, P. W. & PRAY, L. C. 1970. Geologic nomenclature and classification of porosity in sedimentary carbonates. *American Association of Petroleum Geologists Bulletin*, **54**, 207–244.
- CLENNELL, B. 1997. Tortuosity: a guide through the maze. In: LOVELL, M. A. & HARVEY, P. K. (eds) *Developments in Petrophysics*. Geological Society, London, Special Publications, **122**, 299–344.
- CLERKE, E. A., MUELLER, H. W., PHILLIPS, E. C., EYVAZ-ZADEH, R. Y., JONES, D. H., RAMAMOORTHY, R. & SRISVASTAVA, A. 2008. Application of Thomeer Hyperbolas to decode the pore systems, facies and reservoir properties of the Upper Jurassic Arab D Limestone, Ghawar Field, Saudi Arabia: a 'rosetta stone' approach. *GeoArabia*, **13**, 113–160.
- COKER, D. A. & TORQUATO, S. 1995. Extraction of morphological quantities from a digitized medium. *Journal of Applied Physics*, **77**, 6087–6099.
- DEHGHAN KHALILI, A., ARNS, C. H. ET AL. 2013a. Permeability upscaling for carbonates from the pore scale by use of multiscale X-ray-CT images. *SPE/EAGE European Unconventional Resources Conference and Exhibition*, Vienna, Austria, 20–22 March 2012.
- DEHGHAN KHALILI, A., YANICI, S., CINAR, Y. & ARNS, C. H. 2013b. Formation factor for heterogeneous carbonate rocks using multi-scale X-ray-CT images. *Journal of Engineering Research*, **1**, 5–28.
- DOUSSARD, P. A., CECILIA, A. ET AL. 2012. A versatile indirect detector design for hard X-ray microimaging. *Journal of Instrumentation*, **7**, P09016.
- DULLIEN, F. A. L. 1979. *Porous Media: Fluid Transport and Pore Structure*. Academic Press, New York.
- ESTEBAN, M. 1979. Significance of the upper Miocene reefs in the Western Mediterranean. *Paleogeography, Palaeoclimatology, Palaeoecology*, **29**, 169–188.
- GARING, C. 2011. *Caractérisation géophysique et géochimique des interactions fluide-roche à l'interface eau douce-eau salée: cas des carbonates récifaux de Majorque*. PhD thesis, University of Montpellier 2, Montpellier.
- GARING, C., LUQUOT, L., PEZARD, P. A. & GOUZE, P. 2013a. Geochemical investigations of saltwater intrusion into the coastal carbonate aquifer of Mallorca, Spain. *Applied Geochemistry*, **39**, 1–10.
- GARING, C., LUQUOT, L., PEZARD, P. A. & GOUZE, P. 2013b. Electrical and flow properties of highly heterogeneous carbonate rocks. *American Association of Petroleum Geologists Bulletin*, **98**, 49–66, <http://dx.doi.org/10.1306/05221312134>
- GOUZE, P. & LUQUOT, L. 2011. X-ray microtomography characterization of porosity, permeability and reactive surface changes during dissolution. *Journal of Contaminant Hydrology*, **120–121**, 45–55.
- GOUZE, P., MELEAN, Y., LE BORGNE, T., DENTZ, M. & CARRERA, J. 2008. Non-Fickian dispersion in porous media explained by heterogeneous microscale matrix diffusion. *Water Resources Research*, **44**, 11416, <http://dx.doi.org/10.1029/2007WR006690>
- GOUZE, P., LEPROVOST, R., POIDRAS, T., LE BORGNE, T., LODS, G. & PEZARD, P. A. 2009. CoFIS and TELog: New downhole tools for characterizing dispersion processes in aquifers by single-well injection-withdrawal tracer tests. *Comptes Rendus Geoscience*, **341**, 965–975.

- HEBERT, V. 2011. *Analyses multi-échelles de la structure d'un réservoir carbonaté littoral: exemple de la plateforme de Llucmajor (Majorque, Espagne)*. PhD thesis, University of Montpellier 2, Montpellier.
- HOLLIS, C., VAHRENKAMP, V., TULL, S., MOOKERJEL, A., TABERNER, C. & HUANG, Y. 2010. Pore system characterization in heterogeneous carbonates: an alternative approach to widely-used rock-typing methodologies. *Marine and Petroleum Geology*, **27**, 772–793.
- JAEGLI, D. 2006. *Multiscalar porosity structure of a Miocene reefal carbonate complex*. PhD thesis, ETH, Zurich.
- JIANG, Z., VAN DIJKE, M. I. J., GEIGER, S., KRONBAUER, D., MANTOVANI, I. F. & FERNANDES, C. P. 2013a. *Impact of the spatial correlation of microporosity on fluid flow in carbonate rocks*. SPE Reservoir Characterization and Simulation Conference and Exhibition, Abu Dhabi, UAE, 16–18 September 2013, <http://dx.doi.org/10.2118/166001-MS>
- JIANG, Z., VAN DIJKE, M. I. J., SORBIE, K. S. & COUPLES, G. D. 2013b. Representation of multiscale heterogeneity via multiscale pore networks. *Water Resources Research*, **49**, 5437–5449, <http://dx.doi.org/10.1002/wrcr.20304>
- KLINKENBERG, L. J. 1941. The permeability of porous media to liquids and gases. *In: API Drilling and Production Practice. API 11th Mid-Year Meeting*, Tulsa, OK, May 1941. American Petroleum Institute, Washington, DC, 200–213.
- KNACKSTEDT, M. A., SOK, R. M. *ET AL.* 2008. Probing pore systems in carbonates: correlations to petrophysical properties. *SPWLA 49th Annual Logging Symposium*. Edinburgh, Scotland, 25–28 May 2008.
- LINDQUIST, W. B., VENKATARAMAN, A., DUNSMUIR, J. & WONG, T. F. 2000. Pore and throat size distributions measured from synchrotron X-ray tomographic images of Fontainebleau sandstones. *Journal of Geophysical Research: Solid Earth*, **105**(B9), 21 509–21 527.
- LONOX, A. 2006. Making sense of carbonate pore system. *American Association of Petroleum Geologists Bulletin*, **90**, 1381–1405.
- LUCIA, F. J. 1983. Petrophysical parameters estimated from visual descriptions of carbonate rocks: a field classification of carbonate pore space. *Journal of Petroleum Technology*, **35**, 629–637.
- LUCIA, F. J. 1995. Rock-fabric/petrophysical classification of carbonate pore space for reservoir characterization. *American Association of Petroleum Geologists Bulletin*, **79**, 1275–1300.
- LUQUOT, L. & GOUZE, P. 2009. Experimental determination and permeability changes induced by injection of CO₂ into carbonate rocks. *Chemical Geology*, **265**, 148–159.
- LUQUOT, L., RODRIGUEZ, O. & GOUZE, P. 2013. Experimental characterization of porosity structure and transport properties changes in limestone undergoing different dissolution regimes. *Transport in Porous Media*, **101**, 507–532, <http://dx.doi.org/10.1007/s11242-013-0527-4>
- MARIA-SUBE, Y. 2008. *Structure et hétérogénéité d'une plateforme récifale Miocène (Majorque), implication pour les intrusions d'eau salée en zone côtière*. PhD thesis, University of Montpellier 2, Montpellier.
- MANGANE, P. O., GOUZE, P. & LUQUOT, L. 2013. Permeability impairment of a limestone reservoir triggered by heterogeneous dissolution and particles migration during CO₂-rich injection. *Geophysical Research Letters*, **40**, 4614–4619.
- MAZZULLO, S. J. & CHILINGARIAN, G. V. 1992. Diagenesis and origin of porosity. *Developments in Petroleum Science*, **30**, 199–270.
- MEHMANI, A. & PRODANOVIC, M. 2014. The effect of microporosity on transport properties in porous media. *Advances in Water Resources*, **63**, 104–119.
- MEIJSTER, A., ROERDINK, J. B. T. M. & HESSELINK, W. H. 2000. A general algorithm for computing distance transforms in linear time. *In: GOUTSIAS, J., VINCENT, L. & BLOOMBERG, D. S. (eds) Mathematical Morphology and Its Application to Image and Signal Processing*. Computational Imaging and Vision, **18**. Springer, Berlin, 331–340.
- MIRONE, A., GOULLART, E., BRUN, E., TAFFOREAU, P. & KIEFFER, J. 2013. *PyHST2: an hybrid distributed code for high speed tomographic reconstruction with iterative reconstruction and a priori knowledge capabilities*. <https://forge.epn-campus.eu/html/pyhst2/32/index.html>
- MOORE, C. H. 2001. *Carbonate Reservoirs, Porosity Evolution and Diagenesis in a Sequence Stratigraphic Framework*. Developments in Sedimentology, **55**. Elsevier, Amsterdam.
- MOSTAGHIMI, P., BLUNT, M. J. & BIJELIC, B. 2013. Computations of absolute permeability on micro-CT images. *Mathematical Geosciences*, **45**, 103–125.
- MYLROIE, J. E. & CAREW, J. L. 2003. Karst development on carbonate islands. *Speleogenesis and Evolution of Karst Aquifers*, **1**, 21.
- NIMMO, J. R. 2004. Porosity and pore size distribution. *In: HILLEL, D. (ed.) Encyclopedia of Soils in the Environment*. Elsevier, London, **3**, 295–303.
- NOGUES, J. P., FITTS, J. P., CELIA, M. A. & PETERS, C. A. 2013. Permeability evolution due to dissolution and precipitation of carbonates using reactive transport modeling in pore networks. *Water Resources Research*, **49**, 6006–6021.
- NOIRIEL, C., BERNARD, D., GOUZE, P. & THIBAUT, X. 2005. Hydraulic properties and microgeometry evolution accompanying limestone dissolution by acidic water. *Oil & Gas Science and Technology*, **60**, 177–192.
- NOIRIEL, C., LUQUOT, L., MADÉ, B., RAIMBAULT, L., GOUZE, P. & VAN DER LEE, J. 2009. Changes in reactive surface area during limestone dissolution: an experimental and modelling study. *Chemical Geology*, **265**, 160–170.
- PEZARD, P. A., GAUTIER, S., LE BORGNE, T., LEGROS, B. & DELTOMBE, J. L. 2009. MuSET: a multiparameter and high precision sensor for downhole spontaneous electrical potential measurements. *Comptes Rendus Geoscience*, **341**, 957–964.
- POMAR, L. 2001. Ecological control of sedimentary accommodation: evolution from a carbonate ramp to rimmed shelf, Upper Miocene, Balearic Islands. *Palaeontology*, **175**, 249–272.
- POMAR, L. & WARD, W. C. 1999. Reservoir-scale heterogeneity in depositional packages and diagenetic patterns on a reef-rimmed platform, Upper Miocene,

MULTI-SCALE X-RAY TOMOGRAPHY ANALYSIS

- Mallorca, Spain. *American Association of Petroleum Geologists Bulletin*, **83**, 1759–1773.
- POMAR, L., WARD, W. C. & GREEN, D. G. 1996. Upper Miocene reef complex of the Lluçmajor area, Mallorca, Spain. *SEPM Concepts in Sedimentology and Paleontology*, **5**, 191–225.
- PRODANOVIĆ, M., MEHMANI, A. & SHEPPARD, A. P. 2014. Imaged-based multiscale network modelling of microporosity in carbonates. In: AGAR, S. M. & GEIGER, S. (eds) *Fundamental Controls on Fluid Flow in Carbonates: Current Workflows to Emerging Technologies*. Geological Society, London, Special Publications, **406**. First published online June 4, 2014, <http://dx.doi.org/10.1144/SP406.9>
- REMEYSEN, K. & SWENNEN, R. 2008. Application of microfocus computed tomography in carbonate reservoir characterization: possibilities and limitations, 2008. *Marine and Petroleum Geology*, **25**, 486–499.
- SADHUKHAN, S., GOUZE, P. & DUTTA, T. 2012. Porosity and permeability changes in sedimentary rocks induced by injection of reactive fluid: A simulation model. *Journal of Hydrology*, **450–451**, 134–139.
- STAUFFER, D. & AHARONY, A. 1994. *Introduction to Percolation Theory*. Taylor & Francis, London.
- VAN DER LAND, C., WOOD, R., WU, K., VAN DIJKE, M. I. J., JIANG, Z., CORBETT, P. M. W. & COUPLES, G. 2013. Modelling the permeability evolution of carbonate rocks. *Marine and Petroleum Geology*, **48**, 1–7.
- VAN DER MARCK, S. C. 1996. Network approach to void percolation in a pack of unequal spheres. *Physical Review Letters*, **77**, 1785–1788.
- VARLOTEAUX, C., BEKRI, S. & ADLER, P. M. 2013. Pore network modelling to determine the transport properties in presence of a reactive fluid: from pore to reservoir scale. *Advances in Water Resources*, **53**, 87–100.
- VERWER, K., EBERLI, G. P. & WEGER, R. J. 2011. Effects of pore structure on electrical resistivity in carbonates. *American Association of Petroleum Geologists Bulletin*, **95**, 175–190.
- VIALLE, S. & VANORIO, T. 2011. Laboratory measurements of elastic properties of carbonate rocks during injection of reactive CO₂-saturated water. *Geophysical Research Letters*, **38**, L01302, <http://dx.doi.org/10.1029/2010GL045606>
- VIALLE, S., DVORKIN, J. & MAVKO, G. 2013. Implications of pore microgeometry heterogeneity for the movement and chemical reactivity of CO₂ in carbonates. *Geophysics*, **78**, L69–L86.
- WEGER, R. J., EBERLI, G. P., BAECHELE, G. T., MASSAFERRO, J. L. & SUN, Y. 2009. Quantification of pore structure and its effect on sonic velocity and permeability in carbonate. *American Association of Petroleum Geologists Bulletin*, **93**, 1297–1317.
- ZARETSKIY, Y., GEIGER, S., SORBIE, K. & FORSTET, M. 2010. Efficient flow and transport simulations in reconstructed 3D pore geometries. *Advanced in Water Resources*, **3**, 1508–1516.